Research Article Vol. 30, No. 6 / 14 Mar 2022 / Optics Express 8829
Optics EXPRESS

Blazed grating enables highly decoupled optically variable devices fabricated by vibration-assisted diamond texturing

JIANJIAN WANG,[1,2,3] YAOKE WANG,[2] JIANFU ZHANG,[1] VOLKER SCHULZE,[3] AND PING GUO[2,*]

[1]Department of Mechanical Engineering, Tsinghua University, Beijing 100084, China
[2]Department of Mechanical Engineering, Northwestern University, Evanston 60208, USA
[3]Institute of Production Science, Karlsruhe Institute of Technology, Karlsruhe 76021, Germany
*ping.guo@northwestern.edu

Abstract: Optically variable devices (OVDs) are well received for anti-counterfeiting and decorative applications. In this study, new strategies to develop highly decoupled OVDs were proposed and demonstrated based on the fast patterning of blazed gratings by vibration-assisted diamond texturing. A unique surface generation mechanism was revealed as a combined cutting and forming process. One facet of blazed grating is generated by the cutting motion defined by the tool tip trajectory. The other facet is formed by the tool flank face, which establishes the blaze angle. This process is able to generate high-resolution, structurally colored graphics by modulating cutting velocity to control the grating distribution. Due to the unique surface generation mechanism, the orientation of the created blazed gratings is intrinsically perpendicular to the cutting direction. Thus, it enables the flexible control of concentration directions of diffracted light by tuning the orientation of blazed gratings. We designed and demonstrated two types of highly decoupled OVDs based on vibration-induced blazed gratings. The orthogonal-type OVD utilizes the azimuth angle dependence of blazed gratings to encode two images in orthogonal cutting directions. The in-plane-type OVD utilizes the optimized diffraction efficiency of blazed gratings in a given diffraction order to encode two images in opposite cutting directions. The fabricated OVDs are presented and compared with optical simulation results based on an extended scalar diffraction theory.

1. Introduction

An optically variable device (OVD) is a security element that exhibits multiple channels of information, such as color shift or image switch. When an OVD is observed from different viewing angles or illuminated with different lighting conditions, the apparent graphic information will be selectively displayed. Since OVDs cannot be easily photocopied or replicated, they have been adopted as a highly effective measure in anti-counterfeiting and security applications, such as banknotes, official security papers, passports, and credit cards [1]. In addition, OVDs are well received in the market of functional decoration and packaging due to their unique visual effects [2]. The principle of OVDs mainly relies on diffractive optical structures, which utilize a well-controlled distribution of micro/nano features to tune the reflection spectrum of incident light through interference [3,4].

The fabrication of OVDs usually relies on e-beam lithography and laser-beam writing [4]. E-beam lithography is suitable for high-level security applications due to its attainable structural complexity and quality as well as associated high fabrication cost [5]. However, the strict processing conditions and expensive equipment of lithography limit its broader commercial applications. Laser-beam writing, represented by femtosecond laser structuring [6] and laser interference patterning [7], is attractive for industrial applications for both security and decoration

#450628 https://doi.org/10.1364/OE.450628
Journal © 2022 Received 6 Dec 2021; revised 13 Feb 2022; accepted 15 Feb 2022; published 2 Mar 2022

Optics EXPRESS

purposes due to its high material adaptability and production efficiency. Laser structuring and patterning further improve the process efficiency by overcoming the serial fabrication of individual features associated with conventional laser ablation. However, the low controllability of the grating profile results in low optical efficiency and poor fabrication accuracy of OVDs [8].

The optical quality of OVDs strongly depends on the diffraction efficiency of surface gratings. Diffraction efficiency defines how much incident optical power is diffracted into a selected direction [9]. For the applications of gratings in OVDs, the diffraction efficiency is maximized to achieve a better optical effect [10]. Blazed gratings are designed to achieve the maximum diffraction efficiency for the wavelength of the used light, as high as 100% [11]. Blazed gratings have a triangular, saw-toothed profile with a tilted facet, which forms a so-called blaze angle with respect to the grating surface. Compared with other common types of gratings, such as holographic and binary gratings, blazed gratings are capable of concentrating more optical energy in a given non-zeroth diffraction order, which can enable the selective demonstration of color information. The high diffraction efficiency of blazed gratings makes them ideal candidates to implement high-quality OVDs.

Currently, uniform blazed gratings are dominantly fabricated by either the hybrid process of holographic laser lithography and ion beam etching or by mechanical ruling [12]. The former first utilizes holographic laser lithography to create ordinary gratings on a photoresist. It then uses an inclined ion beam to etch the substrate to generate the profile of blazed gratings [13]. This lithography-based method has the advantage of high fabrication efficiency, especially for large-area grating devices. However, it is almost impossible for this method to generate blazed gratings with adjustable spacing at a pixel level, which greatly restricts its application flexibility in OVD fabrication. Mechanical ruling is the standard process to machine high-quality blazed gratings [14]. The process is schematically shown in Fig. 1(a). Uniform gratings are machined along the ruling direction, while the grating profile is a replica of the tool geometry [15]. However, it is difficult to tune the grating spacing at a pixel level in the ruling operation, which makes it unrealistic to directly adopt mechanical ruling for fabricating OVDs.

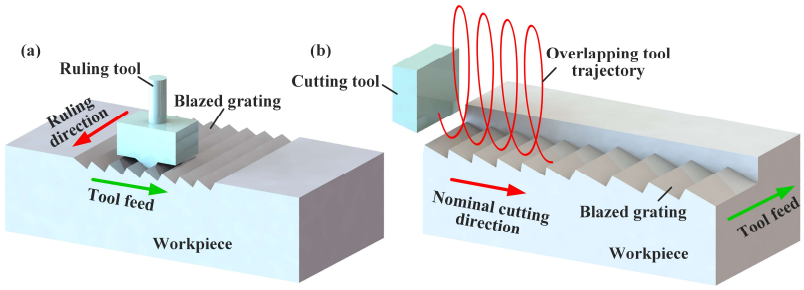

Fig. 1. Comparison of two mechanical machining methods for generating blazed gratings: **a** conventional ruling and **b** proposed vibration-assisted texturing.

Another potential fabrication technique of blazed gratings for OVDs is single-point diamond texturing with the assistance of tool spindle rotation or multi-dimensional mechanical vibrations. Through the tool spindle rotation, the fly cutting can be used to generate grating-type microstructures by replicating the tool geometry [16]. It can program the grating spacing pixel-by-pixel by changing the feed rate [17]. However, fly cutting is restricted by its low generation rate (typically only 50 Hz for a spindle speed of 3000 rpm [18]. In contrast, the vibration assisted texturing process can generate submicron-scale structures with an extremely high efficiency owing to the utilization of high-frequency tool vibration (several kHz to 30 kHz) [19]. This technique has emerged as a novel, promising method for the fabrication of diffractive optical microstructures. Grating-type surface microstructures have been successfully fabricated by diamond texturing

Optics EXPRESS

on various kinds of ductile and brittle materials [20] to provide an iridescent color effect [17]. Recently, vibration-assisted diamond texturing has also been utilized to fabricate two-channel OVDs by carefully programming the grating spacing to utilize the intensity distribution of a diffractive light field of 1D gratings [21]. However, the original vibration-assisted diamond texturing is not able to create blazed grating geometry. The generated uncontrolled grating profile results in low diffraction efficiency and low optical decoupling, which limits the achievable visual quality.

This paper investigates the grating formation mechanism in vibration-assisted diamond texturing and proposes a control strategy to form blazed grating profiles. Based on the blazed grating generation, two new types of highly decoupled OVDs were designed and prototyped. The blazed grating formation mechanism was investigated experimentally to explore how the tool vibration trajectory and tool geometry determine the grating profile. Pixelated blazed gratings with controlled profiles and variable spacing from one to five microns were successfully generated on metallic surfaces with an average surface writing speed of 0.4 mm^2/s. Two new OVD design strategies were demonstrated utilizing the directional light concentration of blazed gratings to achieve orthogonal and in-plane decoupling.

2. Surface generation mechanism of blazed gratings

2.1. Vibration-assisted texturing with a combined cutting and forming process

Different from a ruling process, vibration-assisted texturing utilizes modulated tool trajectories to generate grating-type surface structures. Figure 1 shows the comparison of process principles between a conventional ruling operation and vibration-assisted texturing. As demonstrated in Fig. 1(b), a single crystal diamond tool moves in an elliptical trajectory coupled with a nominal cutting motion. The resultant overlapping tool trajectory results in periodic machined ripples along the cutting path. These machined ripples can be controlled to form conjunctive unit-length gratings with adjustable spacing down to the near-wavelength of the visible spectrum. Since the fabricated grating direction is perpendicular to the cutting direction, the grating spacing can be dynamically adjusted by tuning the cutting velocity or vibration frequency. High-efficiency generation of gratings can be potentially achieved by a high vibration frequency (up to an ultrasonic frequency).

If we intend to control the generated surface structure profile to follow a blazed grating design in vibration-assisted texturing, the surface generation mechanism needs to be further investigated. The pure shearing process in conventional ultraprecision diamond cutting is incapable of generating blazed gratings with a sawtooth profile. We hypothesized a combined cutting and forming process during each tool vibration cycle in vibration-assisted texturing, one which would result in the sawtooth profile formation. As illustrated in Fig. 2(a), each tool vibration cycle can be separated into two half-cycles. In the first half-cycle, the material is removed with the cutting motion to generate the short facet of a blazed grating. In the second half-cycle, the material is compressed by the tool flank to form the long facet of the blazed grating. The critical dimensions of generated blazed gratings are demonstrated in Fig. 2(b), where d, h, and θ are the spacing, height, and blaze angle, respectively; d_b is the length of the blazed facet along the substrate surface.

The dimensions of blazed gratings have deterministic relations to the process parameters in vibration-assisted texturing, including but not limited to the tool vibration trajectories and tool clearance angle. As shown in Fig. 2, the blazed facet is only formed when interference occurs between the tool flank and the machined surface. The condition for creating the blazed facet through compression is determined by the tool clearance angle α and the tool vibration trajectory. So, in the following subsections, the effects of the tool clearance angle and vibration trajectory are experimentally explored to study the surface generation mechanism of blazed grating and to determine an optimized process window.

Optics EXPRESS

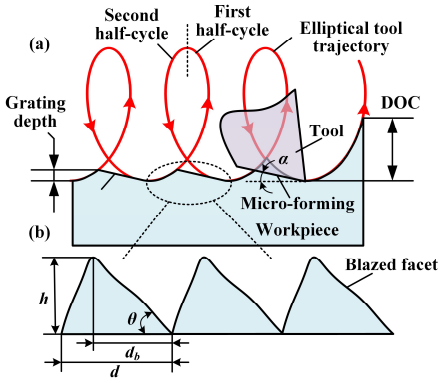

Fig. 2. **a** Surface generation mechanism of blazed grating profile and **b** geometry definition of a blazed grating.

2.2. *Experimental verification on the surface generation mechanism*

In order to verify the proposed surface generation mechanism of blazed grating with elliptical tool vibration, experiments were conducted on an ultraprecision lathe (Nanoform X, Precitech, USA) using two diamond tools with different clearance angles of $\alpha = 10°$ and 45°, respectively (see Appendix A). The other geometric parameters of the diamond tool were kept identical for a rake angle of 0°, an included angle of 60°, and a nose radius of 600 μm. The vibration texturing experiments were divided into two groups for different tool clearance angles, of which the process conditions are listed in Table 1. For each group, the nominal cutting velocity v_c varied from 1 mm/s to 6 mm/s with an increment of 1 mm/s. Since the vibration frequency f was fixed at 2,000 Hz, the generated grating spacing ($d = v_c/f$) varied from 0.5 μm to 3 μm with a step of 0.5 μm. The orientation angle β of the elliptical vibration trajectory was set as 0°, 45°, 90°, and 180°, respectively, while the size of the elliptical trajectory was kept constant with a semi-major axis a of 3 μm and a semi-minor axis b of 1 μm. The machined surfaces were measured by an atomic force microscope (AFM, Bruker Edge, UK). The geometric parameters of blazed gratings were derived from the obtained 3D profile according to the definitions illustrated in Fig. 2(b).

Table 1. Process conditions to explore optimum tool trajectory.

No.	Nominal cutting velocity v_c (mm/s)	Orientation angle of elliptical trajectory β	Vibration parameters	Clearance angle of diamond tool α
1	1, 2, 3, 4, 5, 6	0°, 45°, 90°, 135°	$A = 3$ μm, $b = 1$ μm, $f = 2{,}000$ Hz	10°
2	1, 2, 3, 4, 5, 6	0°, 45°, 90°, 135°	$A = 3$ μm, $b = 1$ μm, $f = 2{,}000$ Hz	45°

The surface profiles of generated gratings for both $\alpha = 10°$ and α=45° at a grating spacing of 2 μm are presented in Fig. 3. As shown in Fig. 3, the successful generation of a blazed facet can be implemented when $\alpha = 10°$ rather than $\alpha = 45°$, indicating that the long blazed facet will only be formed if there is sufficient tool-workpiece interference. When $\alpha = 45°$, a not-well-defined curved profile is generated instead of a straight facet. To clearly demonstrate the differences between the two cases, we defined a dip angle θ' for a straight facet profile to distinguish it from the blaze angle θ as shown in Fig. 3. In particular, when a blazed grating was formed, $\theta' = \theta$.

The influences of the tool clearance angle on the generated dip angle are demonstrated in Fig. 4 for the vibration trajectory ($\beta = 90°$) illustrated in the figure. Only when $\alpha = 10°$ and $d > 1$ μm will the dip angle be approximately equal to the tool clearance angle, indicating that sufficient

Optics EXPRESS

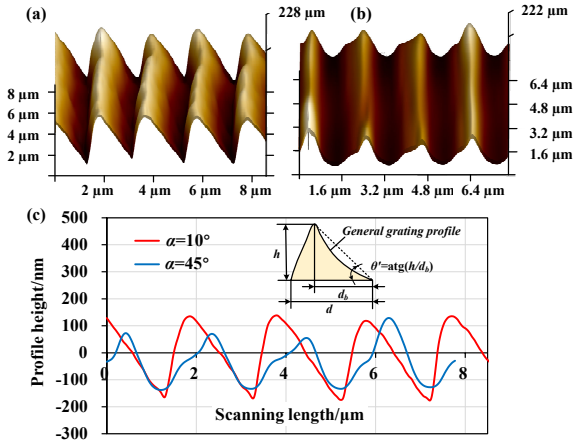

Fig. 3. 3D profile of fabricated grating with different tool clearance angles α at a grating spacing of 2 μm: **a** α=10°, **b** α=45°, **c** cross-section profile.

tool-workpiece interference has occurred, thereby enabling the successful generation of blazed gratings. As shown in Fig. 4, for both $\alpha = 10°$ and $\alpha = 45°$, the dip angle of generated gratings exhibits an apparent increasing trend as the grating spacing d starts to increase. This is because the elliptical tool trajectory is gradually unfolded with the increase of nominal cutting velocity v_c for a fixed vibration frequency f, resulting in the more rapid increase of generated grating height than grating spacing.

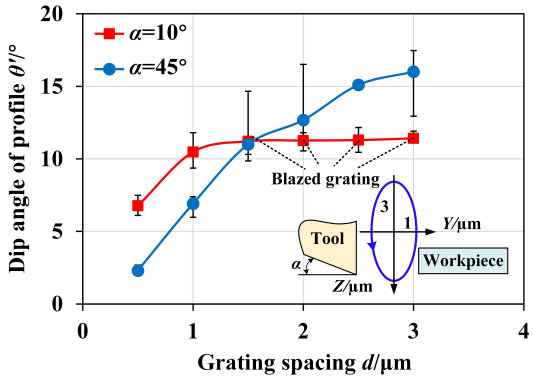

Fig. 4. Effects of grating spacing on the dip angle of fabricated gratings with different tool clearance angles.

However, there are also some important distinctions between the two dip angle curves in Fig. 4. For $\alpha = 45°$, the dip angle always increases as the grating spacing increases. In contrast, for $\alpha = 10°$, the dip angle first significantly increases but then reaches a relatively stable value, as the grating spacing further increases and exceeds 1 μm. This stable value of the dip angle is approximately equal to the tool clearance angle α of 10°, indicating the existence of a forming process in the second vibration cycle. It should be noticed that the stable value of the dip angle is actually slightly larger than 10° due to the spring back of material in the forming process. In summary, the experimental results indicate that the long blazed facet will be formed only if there is sufficient tool-workpiece interference. The hypothetical generation mechanism of blazed grating in vibration-assisted texturing has been verified.

Optics EXPRESS

In addition to the tool clearance angle, the elliptical trajectory is another key factor that affects the generation of blazed gratings. Figure 5(a) shows the effects of the orientation angle β of the elliptical trajectory on the dip angle of generated gratings when the clearance angle $\alpha = 10°$. The variation trends of the dip angle with the grating spacing present a strong dependency on the orientation of the elliptical trajectory. Although the derived dip angle of the grating first increases as the grating spacing increases for every orientation angle β, it can reach a stable value only when β is 45°, 90°, or 135°. These stable values of the dip angle are all near to the tool clearance angle of 10°, demonstrating the existence of the forming process in the second vibration cycle. However, the orientation of the elliptical trajectory significantly determines the achievable spacing range of blazed grating. For $\beta = 45°$ or $\beta = 135°$, the blazed gratings can only be formed when the grating spacing is larger than 2.5 μm. In contrast, when $\beta = 90°$, blazed gratings can be reliably generated starting from the grating spacing of 1 μm. Hence $\beta = 90°$ introduces the most interference in the vibration cycle, which is more desirable in vibration texturing to fabricate blazed gratings.

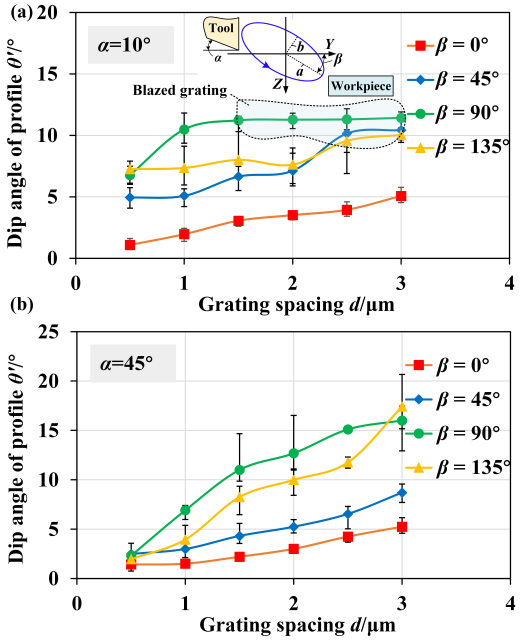

Fig. 5. Effects of the orientation angle β of the elliptical trajectory on the dip angle of fabricated gratings with different tool clearance angles α: **a** $\alpha = 10°$, **b** $\alpha = 45°$.

As a comparison, Fig. 5(b) shows the effects of elliptical trajectory on the dip angle of generated gratings when the clearance angle $\alpha = 45°$. The dip angle always increases with an increase in grating spacing for all orientation angles of the elliptical trajectory. These results indicate that even when using modified or inclined elliptical trajectories, no significant compression occurs between the tool flank and workpiece in the second vibration cycle when the clearance angle $\alpha = 45°$. Hence, in summary, to generate blazed gratings for high-quality OVD fabrication, the following processing window is recommended: a clearance angle $\alpha = 10°$ and an orientation angle of the elliptical trajectory $\beta = 90°$.

It is worthy to note that the proposed method for blazed grating fabrication has its own limitations. Because vibration-assisted texturing is based on diamond cutting, it is difficult to directly texture ferrous and brittle materials, such as ceramics, silicon, and hardened steel.

Optics EXPRESS

The vibration-assisted texturing brings higher flexibility and efficiency compared with the conventional ruling, but gives up precise control over the grating profile. As illustrated in our analysis, the blaze angle of generated gratings cannot be arbitrarily controlled. In addition, the grating height is coupled with the grating spacing, which cannot be independently controlled. The minimal achievable grating spacing is around 300 nm below which the tool sharpness will limit the material removal.

3. Design of highly decoupled OVDs

Blazed gratings are optimized to concentrate the diffracted light in a given direction, which is ideal for OVD decoupling. We propose two encoding strategies to fabricate highly decoupled OVDs, taking advantage of the strong directionality of blazed gratings and our unique process capability to flexibly and efficiently pattern pixelated blazed gratings. The orthogonal-type OVD utilizes the diffraction dependence of the azimuth angle to encode two images in the two orthogonal cutting directions. The in-plane-type OVD utilizes the optimized diffraction efficiency of blazed gratings in a given diffraction order to encode two images in the two opposite cutting directions. An optical simulation model was established to predict the appearance of the designed OVDs based on an extended scalar diffraction theory by considering a general off-plane mount and grating distributions.

3.1. Design of the orthogonal-type OVD

The design principle of the orthogonal-type OVD relies on the orthogonal directionality of blazed gratings. To demonstrate the unique properties of blazed grating, we consider a general off-plane diffraction mount, where the incident and diffracted light rays are not necessarily coplanar. When the incident plane has an angle to the diffraction plane, the diffraction efficiency will be affected by the angle between these two planes, defined as the azimuthal angle ϕ. Figure 6(a) illustrates a general case of an off-plane diffraction mount with the definitions of the azimuthal angle and other important optical angles.

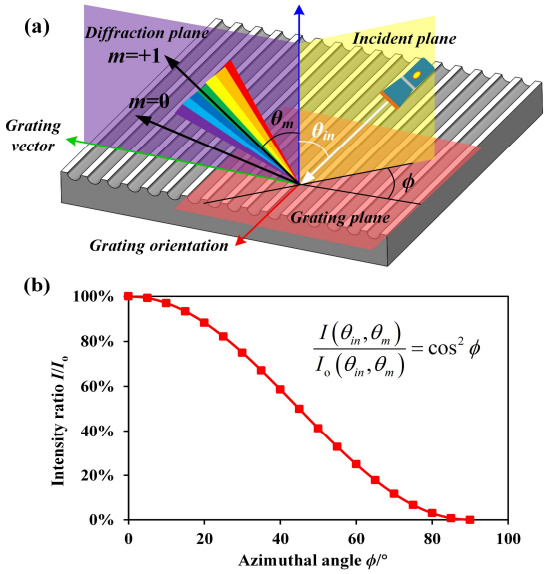

Fig. 6. **a** Schematic of 1D grating diffraction when the incident white light is in a general plane; **b** dependency of the intensity of diffracted light on the azimuthal angle of incident light.

Optics EXPRESS

For the general off-plane mount with an azimuthal angle ϕ, the extended diffraction equation can be expressed as

$$m\lambda = d\left(\sin\theta_m - \frac{\sin\theta_{in}\cos^2\phi}{\sqrt{\sin^2\theta_{in}\cos^2\phi + \cos^2\theta_{in}}}\right) \tag{1}$$

where θ_{in} and θ_m are the incident and diffraction angles of the mth order, which are illustrated in Fig. 6(a). The intensity of dispersed white light is related to the azimuthal angle ϕ. The directionality of 1D grating diffraction is further demonstrated in Fig. 6(b). When ϕ=0°, it is reduced to the classical diffraction mount, so the diffraction intensity reaches its maximum value. When ϕ=90°, the intensity of diffracted white light drops to zero, so no dispersion of white light or structural coloration will be observed in the diffraction plane [22]. The directionality of 1D diffractive grating provides the potential to implement totally decoupled encoding of OVDs by controlling the grating orientations (effectively the azimuthal angle).

The encoding strategy of the orthogonal-type OVD in this study can be summarized as the orthogonal distribution of two groups of blazed gratings. Each group of blazed gratings will be used to encode one channel of graphic information. Two figures, shown in Fig. 7(a) and Fig. 7(b), were selected as the two channels of graphics to be encoded to demonstrate the design principle. The first figure is the emblem of Northwestern University (termed Graphic A), while the second figure is the Northwestern Wildcat logo (termed Graphic B). The pixel-by-pixel encoding strategy is schematically illustrated in Fig. 7(c). The actual grating spacings are in the range of 2.2–4.5 μm. The pixel size is 50 μm × 50 μm.

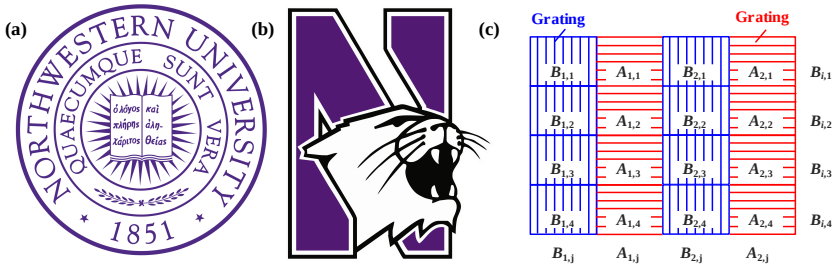

Fig. 7. Two graphics to be encoded in the OVD: **a** Graphic A: the emblem of Northwestern University; **b** Graphic B: the logo of Northwestern Wildcat. **c** Orthogonal decoupling strategy: distribution of gratings with orthogonal orientations.

3.2. Design of the in-plane-type OVD

The design principle of the in-plane-type OVD relies on the in-plane directional light concentration of blazed gratings. In the diffraction plane that is perpendicular to the grating orientation or the classical diffraction mount, the diffracted light concentration also shows strong directionality. As illustrated in Fig. 8(a), for an array of ideal blazed gratings with a blaze angle θ and a spacing d, when the incident light with a wavelength λ is perpendicular to the substrate surface, the diffraction equation can be expressed as

$$d\sin(\theta_{\mathrm{m}} = 2\theta) = \mathrm{m}\lambda \tag{2}$$

When Eq. (2) is satisfied, λ is also called the blaze wavelength. Under this circumstance, most of the light energy is concentrated in the designated direction where $\theta_{\mathrm{m}} = 2\theta$. From Eq. (2), we can see that the grating spacing d can be used to implement a selective concentration of the light with a wavelength λ into the given observation direction, which provides an efficient approach to control the color appearance. Figure 8(b) schematically illustrates the distribution of diffracted

Optics EXPRESS

light intensity for both binary gratings and blazed gratings. We can see that for the ordinary binary grating, the majority of optical power is concentrated on the zeroth diffraction order, which, however, cannot be used for spectrum-related applications, including structural coloration, since there is no light dispersion. For blazed grating, the diffraction intensity is concentrated in the designated direction to achieve structural coloration. In addition, the light intensity distribution is non-symmetric for blazed gratings, where the negative diffraction order ($m < 0$) is much smaller than that in the blaze direction, which helps to achieve optical decoupling in the diffraction plane.

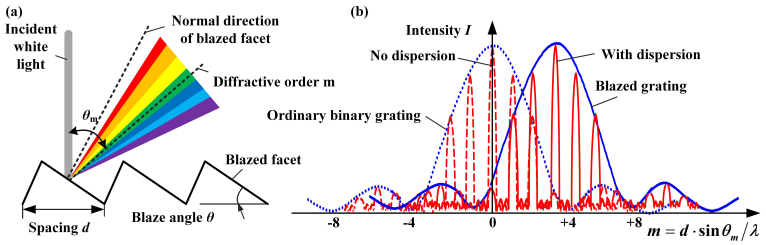

Fig. 8. **a** Diffraction of light induced by blazed grating; **b** comparison of diffraction intensity between ordinary gratings.

As shown in Fig. 8(a), the concentration direction of light energy always shares the same quadrant plane with the normal direction of a blazed facet. The included angle of the concentration direction of light energy and the normal direction of the blazed facet is theoretically equal to the blaze angle θ. Due to the unique surface generation mechanism, the orientation of the created blazed gratings is intrinsically perpendicular to the cutting direction. Since the blazed facets are formed by the tool flank face, the light concentration direction always shares the same quadrant plane with the nominal cutting direction. If we reverse the nominal cutting direction, the light concentration direction will be shifted to the other quadrant plane.

To evaluate the in-plane directionality of fabricated blazed gratings, we machined color blocks in the opposite cutting directions using the proposed vibration-assisted texturing. The design of cutting tests and the observation results of cutting results are illustrated in Fig. 9. The elliptical vibration trajectory adopted the optimal parameters identified in Section 2. The vibration frequency was set at 2,000 Hz and the nominal cutting velocity was 5.0 mm/s. As shown in Fig. 9, three color blocks were created using two opposite nominal cutting directions, respectively. The machining results were observed from two different viewing directions—namely, ψ is equal to $+20°$ or $-20°$. The color blocks fabricated with two opposite cutting directions show distinct brightness, which can be further shifted if the viewing angle ψ is changed from $+20°$ to $-20°$. This is because the light intensity of the negative diffractive order ($m < 0$) is much smaller than that in the blaze direction. These results demonstrated that the fabricated blazed gratings have good directionality, which can be controlled by the nominal cutting direction.

Figure 10 illustrates the design of a two-channel OVD with in-plane decoupling. Two images, namely a cat (Image I) and a mouse (Image II), were encoded into the surface of the OVD. For each image to be encoded, the nominal cutting velocity was changed, pixel by pixel, to modify the grating spacing to selectively concentrate the light of a particular wavelength into the designated observation direction. The determination of grating spacing for each pixel can be derived from the selected light wavelength to be concentrated according to their relationship in Eq. (1) [19]. As demonstrated in Eq. (1), each grating spacing d corresponds to one blaze wavelength λ to be concentrated, which provides an efficient approach to controlling the color appearance of the surface. From Eq. (1), the actual grating spacings are in the range of 2.2–4.5 μm. The pixel size is 50 μm × 50 μm. The viewing angles are designed to be ±20°. As shown in Fig. 10, the nominal cutting directions for the two encoded images are opposite to each other. Due to the

Optics EXPRESS

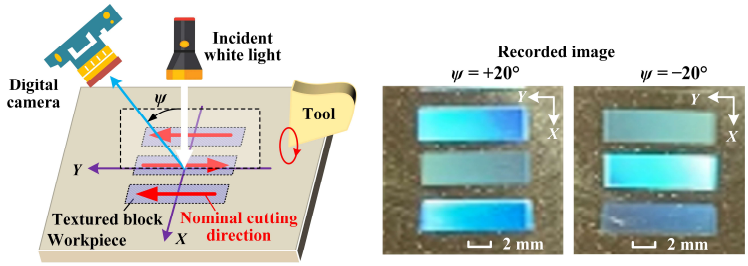

Fig. 9. Evaluation of the directionality of blazed gratings fabricated by vibration-assisted texturing.

unique generation mechanism of blazed gratings, the light concentration direction of blazed gratings always shares the same quadrant plane with the nominal cutting direction. Thus, the optimum observation direction for the two encoded images can be reliably separated when the white incident light is perpendicular to the workpiece surface. Hence, for the designed OVD shown in Fig. 10, when the observation direction changes gradually from right to left, Image I and Image II will appear sequentially.

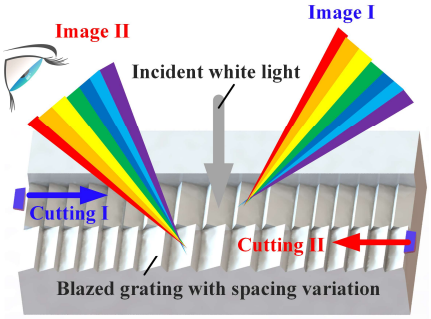

Fig. 10. Design principle of optically variable devices (OVDs) based on blazed grating.

3.3. *Theoretical model to predict the appearance of OVDs*

Considering that the grating equation presented in Eq. (1) cannot describe the superimposed effects of diffracted light by multiple pixels, the model developed in this study utilizes an extended scalar diffraction theory [20] that is able to process the off-plane incident case of diffraction phenomena [23,24]. According to the scalar diffraction theory [25], for the diffractive optical setup shown in Fig. 11(a), the distribution of irradiance intensity I on a plane in the far field of the diffracting aperture can be described as

$$I(\lambda, \theta_{in}) = \cos\theta_{in} |\mathcal{F}\{U(x,y)\}|^2 \tag{3}$$

where θ_{in} is the incident angle of light relative to the normal direction of the grating plane, λ is the wavelength of the light, and x and y are the coordinate components shown in Fig. 11. $U(x, y)$ is the distribution of complex amplitude emerging from the surface of the diffractive aperture, which is described as

$$U(x,y) = \begin{cases} e^{-4\pi i h(x,y)/\lambda} & (x,y) \in A_s \\ 0 & (x,y) \notin A_s \end{cases} \tag{4}$$

Optics EXPRESS

where A_s is the region of a one-pixel diffraction element, $h\,(x, y)$ denotes the surface profile of a one-pixel diffraction element. $\mathcal{F}$ denotes the Fourier transform operation and is defined as

$$\mathcal{F}\{U(x,y)\} = \int_{-\infty}^{\infty}\int_{-\infty}^{\infty} U(x,y)\cdot e^{-2\pi i\left(x\frac{\sin\theta_{in}\cos\phi}{\lambda}+y\frac{\sin\theta_{in}\sin\phi}{\lambda}\right)}\mathrm{d}x\mathrm{d}y \tag{5}$$

Using Eqs. (4) and (5), the light spectrum $I\,(\lambda)$ can be derived. Then, the RGB color conversion can be conducted using [26]:

$$\begin{cases} X = \int_0^{\infty} I(\lambda)\bar{r}(\lambda)\mathrm{d}\lambda \\ Y = \int_0^{\infty} I(\lambda)\bar{g}(\lambda)\mathrm{d}\lambda \quad ,\lambda \in [380, 780] \\ Z = \int_0^{\infty} I(\lambda)\bar{b}(\lambda)\mathrm{d}\lambda \end{cases} \tag{6}$$

where $\bar{r}$, $\bar{g}$, $\bar{b}$ are the CIE 1931 2° standard color-matching functions as shown in Fig. 11, which can be found in [27]. The MATLAB function *xyz2rgb* is used to convert the obtained *XYZ* of each corresponding pixel into the sRGB space, followed by a further scaling to a range of 0–255 for the screen display. The simulation model assumes the ideal grating geometry with the predicted blaze angles. The profile errors induced by the tool geometry and cutting dynamics are not considered.

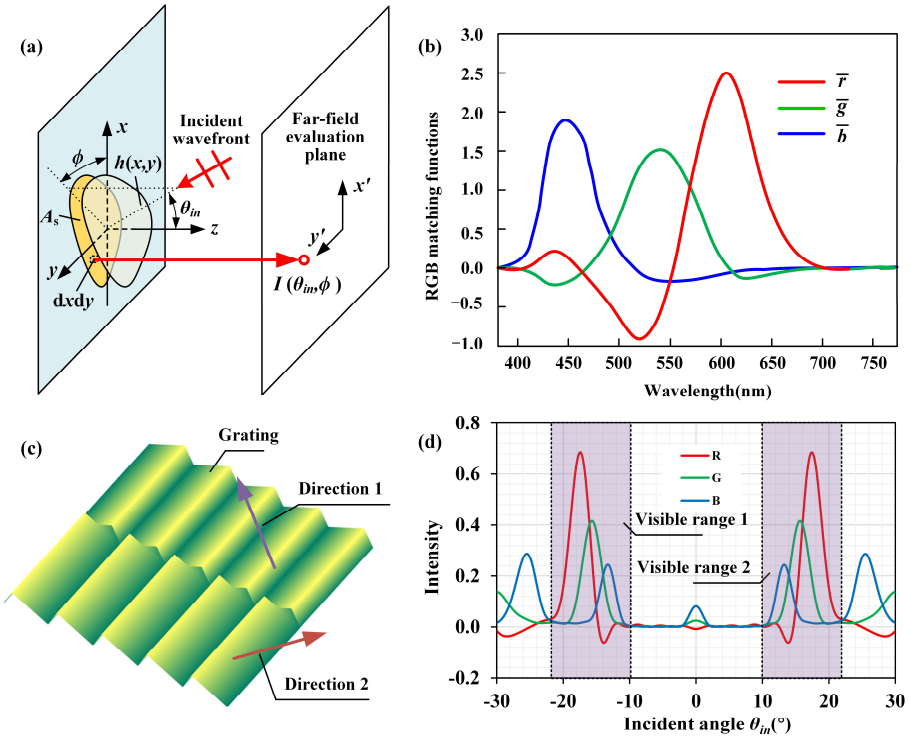

Fig. 11. **a** Geometry for the scalar diffraction setup. **b** CIE 1931 2° color-matching functions converted to RGB weighting functions with a D65 illuminant as a Ref. [27]. **c** Optical structure with opposite grating direction. **d** Intensity of R, G, B from variable incident angles.

As an example, an optical surface structure composing blazed gratings with the same spacing but in the opposite direction is shown in Fig. 11(c). The simulated diffraction intensities for RGB

Optics EXPRESS

light from variable incident angles are plotted in Fig. 12(d), which shows two separate peaks in the positive and negative incident angle range. These two peaks correspond to the diffraction directions for the two opposite gratings, so the diffracted color is spatially decoupled, resulting in the in-plane OVD effect introduced in Section 4.2.

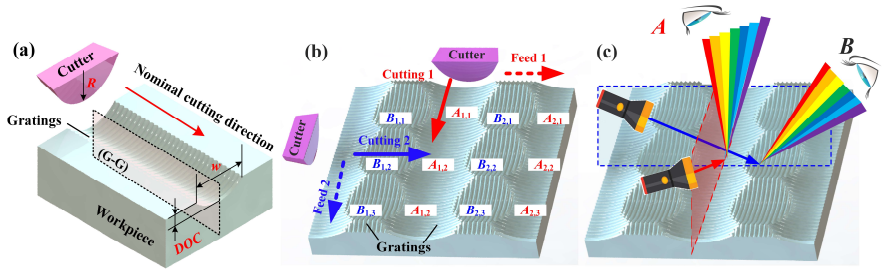

Fig. 12. **a** Illustration of the machined groove using a diamond cutter with a nose radius R. **b** Programming of cutting paths in fabricating orthogonal-type OVDs with vibration-assisted texturing. **c** Displaying principle of the fabricated OVD.

4. Fabrication of highly decoupled OVDs

Vibration-assisted texturing tests on brass workpieces are successfully demonstrated in this section to verify the efficacy of the proposed fabrication strategies of OVDs by utilizing the directional light concentration of blazed gratings. Since the orientation of the created blazed gratings is intrinsically perpendicular to the cutting direction of the diamond tool, the two kinds of designed OVDs are fabricated by rendering different infographics in opposite or orthotropic cutting directions, respectively.

4.1. Fabrication of the orthogonal-type OVD

When fabricating an orthogonal-type OVD, two groups of grating patterns are rendered in the orthogonal directions to render two sets of images. However, the subsequent cutting step in the orthogonal direction might wipe out the microstructures generated in the first cutting step. To guarantee that the grating patterns for the second image (Graphic B) can be reliably created without wiping out the information written in the first step, we adopt a diamond cutter with a circular nose and tune the depth of cut (DOC) in the second cutting step. Since the shape of the generated surface is a replica of the cutter nose, when a circular diamond cutter is used, as shown in Fig. 12(a), the width w of the grooved surface is determined by the cutter nose radius of R and the DOC through the following equation:

$$w = 2\sqrt{R^2 - (R - \mathrm{DOC})^2} \tag{7}$$

As shown in Fig. 12(b), in the first step, the group of blazed grating patterns for displaying Graphic A will be textured along each grooved surface. By modulating the nominal cutting velocity pixel by pixel, the structurally colored Graphic A can be replicated with high resolution. Then, in the second step, the gratings are textured in the orthogonal direction for Graphic B. With a reduced DOC, the tool will not touch the bottom of the grooves created in the first step, thus only partially overwriting the surface to create a second set of gratings. The nominal cutting velocity is also dynamically adjusted to achieve pixel-by-pixel rendering. The tool vibration frequency and trajectory are both kept unchanged during the rendering process. Though there is a slight misalignment error up to half of the grating spacing at the interface of adjacent passes,

Optics EXPRESS

the transitions will still be continuous and not affect the optical appearance of designed OVDs [19]. In Fig. 12(b), $A_{i,j}$ and $B_{m,n}$ represent the pixels with different grating spacing in the two orthogonal directions. Figure 12(c) demonstrates the displaying principle of the fabricated OVD surface. When the OVD is observed from two orthogonal directions, it will only display one rendered image (Graphic *A* or Graphic *B*) to achieve the optically variable effect.

The surface texturing tests to fabricate the orthogonal-type OVD were conducted on an ultra-precision lathe (Nanoform X, Precitech, USA) with the coordinate system defined in Appendix A. The tool vibration trajectory adopted the optimal parameters identified in Section 2. The vibration frequency was set at 2,000 Hz. As shown in Fig. 13(a), the pixel size was set to 100 µm by 100 µm, while the DOCs for the two orthogonal cuts were 4 µm and 1.5 µm, respectively. The difference in DOC was experimentally calibrated to ensure that each image covers 50% of the whole surface. The machined surface with 1D gratings was measured using a 3D laser confocal microscope (OLS5000, Olympus, USA). The optical system used to observe and record the visual effects of the machined surface is schematically shown in Fig. 13(b), in which the incident angle θ_{in} is fixed at 20°, while the azimuthal angle ϕ varies from 0° to 90°.

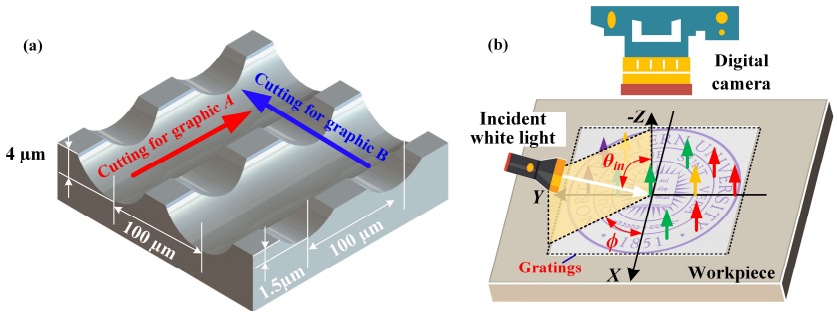

Fig. 13. **a** Illustration of key process parameters, including the DOC and feed, with the designed elliptical trajectory when $f = 2{,}000$ Hz. **b** Observation method of machined results with varying azimuthal angle ϕ and fixed incident angle θ_{in} of 20°.

The experimentally obtained optical images are compared with the model prediction for the designed two-channel OVD under different illuminating conditions, as shown in Fig. 14. The incident angle θ_{in} is fixed as 20°, while the azimuthal angle ϕ varies from 0° to 90°. When the azimuthal angle ϕ is 0°, only Graphic *A*, namely the logo of Northwestern University, can be observed. On the other hand, when the azimuthal angle ϕ is 90°, only Graphic *B*, namely the logo of Northwestern Wildcat, can be observed. Hence, the two encoded graphics have been totally decoupled to show high-quality optically variable visual effects. The experimental results of the optically variable visual effects of the designed OVD agree well with the predicted results of the simulation illustrated in Section 3.3. Moreover, the surface morphology of the selected area of the fabricated OVD is shown in Fig. 15, which distinctly demonstrates the orthogonally distributed two groups of 1D gratings and verifies the feasibility of orthogonal-type OVD design.

4.2. *Fabrication of the in-plane-type OVD*

The fabrication of the in-plane-type OVD was conducted with the proposed vibration-assisted texturing approach on the same experimental setup shown in Fig. 17. The diamond tool with a clearance angle of 10° was used to texture the surface of the brass workpiece. The machining of the OVD was separated into two steps to render the two images (Image I and Image II), respectively. After the rendering of Image I was finished, the workpiece was rotated 180° using the spindle of a lathe to enable the rendering of Image II. In this way, the nominal cutting directions for rendering these two images were opposite to each other. The optical system used

Optics EXPRESS

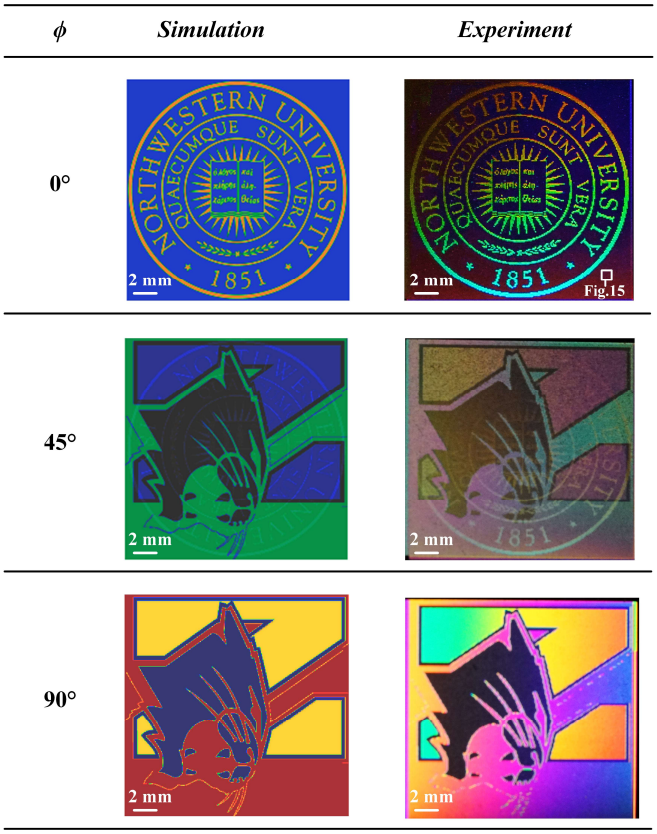

Fig. 14. Results of simulation and experiments of the orthogonal-type OVD (see Visualization 1).

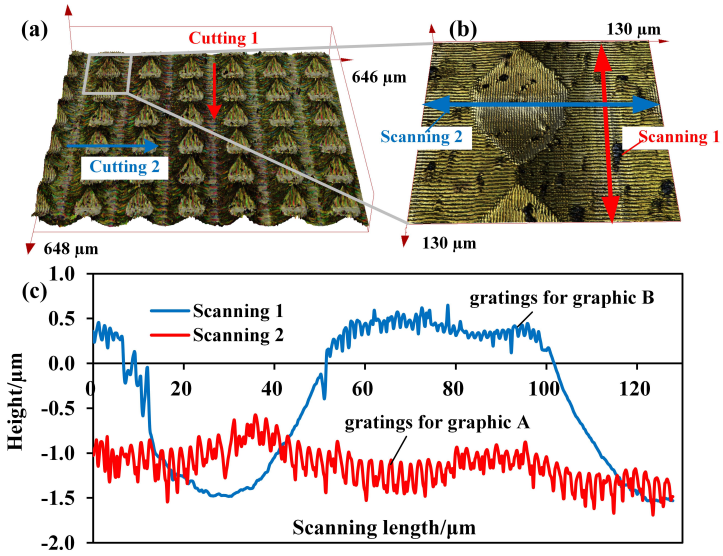

Fig. 15. Surface morphology of the selected area of the fabricated orthogonal-type OVD obtained by 3D laser confocal microscope. **a-b** 3D morphology; **c** cross-section profiles.

Optics EXPRESS

to observe and record the appearance of the fabricated OVD is shown in Fig. 16(a), where the observation angle ψ is set as −20°, 0°, and +20°, respectively.

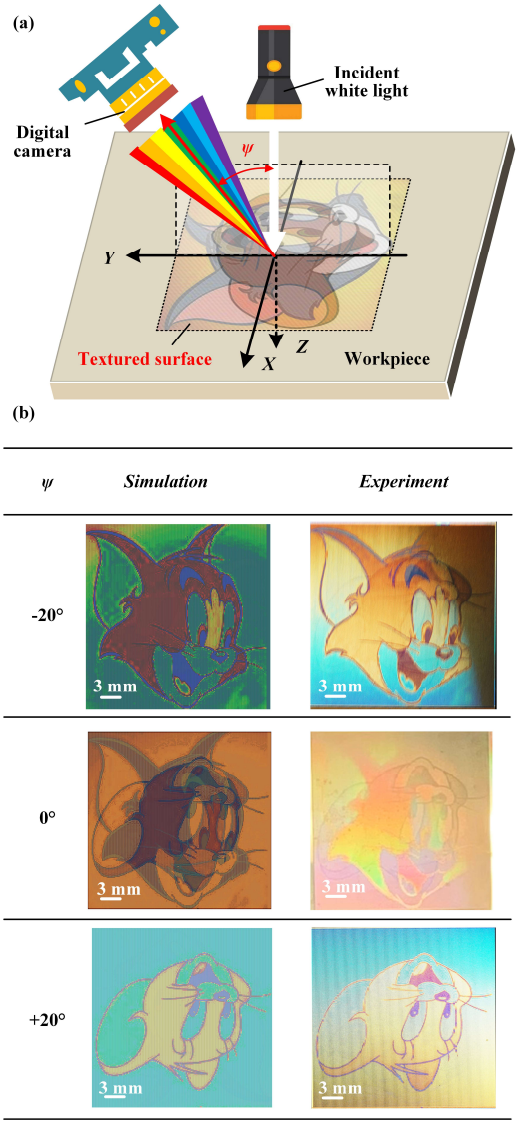

Fig. 16. **a** Optical system to record the appearance of the in-plane OVD; **b** recorded and simulated appearance of the fabricated OVD for different observation angles (see Visualization 2).

Both the predicted and observed visual effects of the designed OVD are presented in Fig. 16(b). As shown in Fig. 16(b), the two encoded images have been well decoupled. When the observation angle ψ is −20° or +20°, only the cat or the mouse can be clearly observed at the designed viewing angle where the diffraction efficiency is at its maximum. The same optically variable phenomenon can also be concluded from the predicted results, verifying the effectiveness of the developed model for the appearance simulation of the OVD. The results presented here can further demonstrate that the vibration-assisted texturing process has an excellent capability in the

Optics EXPRESS

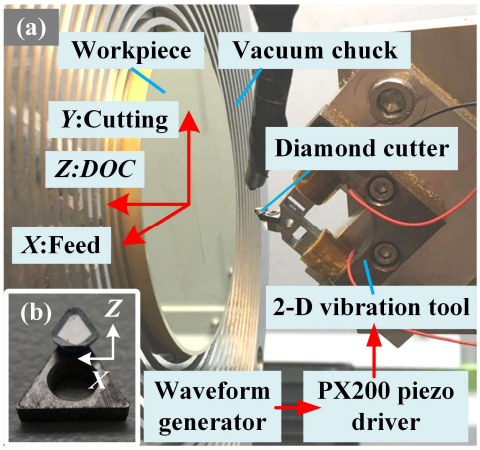

Fig. 17. Experimental setup.

pixel-level control of the microstructure profile. In addition to OVD, the proposed process could also be utilized to texture free-formed optical mirror/lens with blazed gratings for the fabrication of imaging spectrometers with a more compact design.

The process is based on a deterministic mechanical removal process with high repeatability. The grating spacing will be most accurate regardless of the errors discussed below as long as a constant vibration frequency is kept. However, the grating profile accuracy and repeatability will be affected by the vibration trajectory and tool wear. In the current implementation, the piezo-based vibration tool works in an open-loop manner, so the property changes of piezo stacks due to heat accumulation might change the vibration amplitudes, thus affecting the grating formation. The flank wear is another factor that will influence the grating profile. To be noted, the optical appearance is still dominantly determined by the grating spacing, which will not be affected by the error sources. However, the change of grating profile will affect the image rendering quality (color intensity and saturation).

5. Conclusions

In this study, vibration-assisted diamond cutting was adopted to fabricate blazed gratings in the scale of the near-wavelength of visible light. The unique formation mechanism of blazed gratings was revealed and verified experimentally. Two types of highly decoupled optically variable devices (OVDs) were designed and fabricated by utilizing the directional light concentration of blazed gratings. The following conclusions can be drawn.

(1) The surface generation mechanism of blazed gratings in vibration-assisted diamond texturing was revealed as a combined cutting and forming process. In the first-half vibration cycle, the material is cut with chip removal. Then, in the second-half vibration cycle, the material is compressed by the tool flank face to form the saw-toothed profile. A smaller tool clearance angle is more desirable for the successful generation of the blazed facet of the grating.

(2) The orientation of the elliptical tool trajectory is crucial for the surface generation of blazed gratings. For an elliptical trajectory with a semi-major axis of 3 μm and a semi-minor axis of 1 μm, the orientation angle is optimized as 90° to enhance a wider achievable range of grating spacing.

Optics EXPRESS

(3) The design principle of the orthogonal-type OVD utilizes the azimuth angle dependence of blazed gratings to encode two figures in two orthogonal cutting steps. In the second cutting step, the reduced depth of the cut and the circular nose of the diamond cutter are the key process designs for successful grating rendering, avoiding wiping out the gratings written in the first step.

(4) The in-plane-type OVD utilizes the optimized diffraction efficiency of blazed gratings in a given diffraction order to encode two figures in opposite cutting directions. By precisely controlling the nominal cutting directions opposite to each other, a highly decoupled two-channel OVD can be fabricated.

(5) The optical appearance of the designed OVDs is predicted based on an extended scalar diffraction model. The experimental results of the optical appearance of machined OVDs agree well with the simulation results, further verifying the efficacy of the vibration texturing process in the fabrication of blazed gratings.

Appendix A. Machining platform description

As shown in Fig. 17(a), the utilized lathe has three linear axes (XYZ) and a rotational axis (spindle). The linear axes are used to generate servo motions of the tool relative to the workpiece, while the spindle is indexed to precisely control the workpiece orientation. The brass workpiece is fixed on the lathe using a vacuum chuck and pre-turned before texturing to ensure a flat surface. A 2D non-resonant vibration cutting tool, which can work at 2,000 Hz with a full stroke space of 16 μm × 15 μm, is adopted to perform vibration-assisted texturing [28]. High-efficiency fabrication of sub-micrometer gratings can be achieved by utilizing this non-resonant tool (at the rate of 2,000 gratings per second), which could be easily extended to the ultrasonic frequency with a resonant-type vibration tool for even higher process efficiency. The patterning rate in mm^2/s can be calculated by multiplying the nominal cutting velocity by the cutting width. For a nominal cutting velocity of 6 mm/s and a cutting width of 50 μm, the patterning rate is 0.3 mm^2/s. If we adopt an ultrasonic vibration cutting tool, the patterning rate can be further increased by tenfold to 3 mm^2/s (assuming a vibration frequency of 2 kHz). The vibration cutting tool is actuated by two piezo drivers (PX200, PiezoDrive, Australia), which amplifies sinusoidal signals from a waveform generator (TG5011A, Thurlby Thandar Instruments, USA). As shown in Fig. 17(b), a diamond cutter (Contour Fine Tooling, UK) with a nose radius R of 600 μm, a rake angle of 0°, and a clearance angle of 10° is utilized for vibration-assisted texturing. An oil-based lubricant is used during the texturing process.

Funding. McCormick School of Engineering, Northwestern University (Start-up fund); National Natural Science Foundation of China (51761145103); Beijing Municipal Natural Science Foundation (3222009).

Acknowledgments. This work made use of the NUFAB facility of Northwestern University's NUANCE Center, which has received support from the SHyNE Resource (NSF ECCS-2025633), the IIN, and Northwestern's MRSEC program (NSF DMR-1720139). The first author would like to acknowledge the fellowship support from the Alexander von Humboldt Foundation.

Disclosures. The authors declare no conflicts of interest.

Data availability. Data underlying the results presented in this paper are not publicly available at this time but may be obtained from the authors upon reasonable request.

References

1. R. A. Lee, "Micro-technology for anti-counterfeiting," Microelectron. Eng. **53**(1-4), 513–516 (2000).
2. L. Chen, N. Chen, Y. Li, W. Li, X. Zhou, Z. Wang, Y. Zhao, and Y. Bu, "Metal-dielectric pure red to gold special effect coatings for security and decorative applications," Surf. Coat. Technol. **363**, 18–24 (2019).
3. W. R. Tompkin, A. Schilling, C. Weiteneder, and H. P. Herzig, "Zero-order gratings for optically variable devices," Optical Security and Counterfeit Deterrence Techniques IV. International Society for Optics and Photonics **4677**, 227–237 (2002).

Optics EXPRESS

4. R.A. Lee, *Micromanufacturing for document security: optically variable devices*. (Springer Berlin Heidelberg, Berlin, Heidelberg, 2006), pp. 131–169.
5. Y. Heo, H. Kang, J. Lee, Y. Oh, and S. Kim, "Lithographically encrypted inverse opals for anti-counterfeiting applications," Small **12**(28), 3819–3826 (2016).
6. A. Y. Vorobyev and C. Guo, "Colorizing metals with femtosecond laser pulses," Appl. Phys. Lett. **92**(4), 041914 (2008).
7. F. Rößler, T. Kunze, and A. F. Lasagni, "Fabrication of diffraction based security elements using direct laser interference patterning," Opt. Express **25**(19), 22959–22970 (2017).
8. M. S. Sidhu, P. Munjal, and K. P. Singh, "High-fidelity large area nano-patterning of silicon with femtosecond light sheet," Appl. Phys. A **124**(1), 46 (2018).
9. I. K. Baldry, J. Bland Hawthorn, and J. G. Robertson, "Volume phase holographic gratings: polarization properties and diffraction efficiency," Publ. Astron. Soc. Pac. **116**(819), 403–414 (2004).
10. S. Storm, S. Alamri, M. Soldera, T. Kunze, and A.F. Lasagni, "How to tailor structural colors for extended visibility and white light generation employing direct laser interference patterning," Macromol. Chem. Phys. **220**(13), 1900205 (2019).
11. K. M. Harrison, *Grating spectroscopes and how to use them (Vol. 4)*. Springer Science & Business Media. (2012).
12. M. Mattelin, A. Radosavljevic, J. Missinne, D. Cuypers, and G. Van Steenberge, "Design and fabrication of blazed gratings for a waveguide-type head mounted display," Opt. Express **28**(8), 11175–11190 (2020).
13. T. Harada, H. Sakuma, and M. Fuse, "Fabrication of blazed gratings and grisms utilizing anisotropic etching of silicon," Theory and Practice of Surface-Relief Diffraction Gratings: Synchrotron and Other Applications. International Society for Optics and Photonics **3450**, 11–16 (1998).
14. X. Mi, H. Yu, H. Yu, S. Zhang, X. Li, X. Yao, X. Qi, and Q. Wan, "Correcting groove error in gratings ruled on a 500-mm ruling engine using interferometric control," Appl. Opt. **56**(21), 5857–5864 (2017).
15. X. Jirigalantu, X. Li, K. Mi, Y. Liu, and Tang, "Development of a parameterized mechanical model of a chisel-edge grating ruling tool," Precis. Eng. **50**, 388–392 (2017).
16. T. Zhou, Y. He, T. Wang, X. Dong, P. Liu, W. Zhao, Y. Hu, and J. Yan, "Algorithm of micro-grooving and imaging processing for the generation of high-resolution structural color images," Nanomanuf. Metrol. **3**(3), 187–198 (2020).
17. Y. He, T. Zhou, X. Dong, P. Liu, W. Zhao, X. Wang, Y. Hu, and J. Yan, "Generation of high-saturation two-level iridescent structures by vibration-assisted fly cutting," Mater. Des. **193**, 108839 (2020).
18. Y. Yang, Y. Pan, and P. Guo, "Structural coloration of metallic surfaces with micro/nano-structures induced by elliptical vibration texturing," Appl. Surf. Sci. **402**, 400–409 (2017).
19. Y. He, T. Zhou, X. Dong, Z. Zhu, Q. Yu, P. Liu, W. Zhao, X. Wang, Y. Hu, and J. Yan, "Diffraction manipulation of visible light with submicron structures for structural coloration fabrication," Opt. Express **29**(6), 9294 (2021).
20. J. Wang, Y. Wang, Y. Yang, J. Zhang, and P. Guo, Structural coloration of nonmetallic surface using ductile-regime vibration-assisted ultraprecision texturing, Light: Advanced Manufacturing (2021), accepted.
21. P. Guo and Y. Yang, "A novel realization of diffractive optically variable devices using ultrasonic modulation cutting," CIRP Ann. **68**(1), 575–578 (2019).
22. T. Jwad, P. Penchev, V. Nasrollahi, and S. Dimov, "Laser induced ripples' gratings with angular periodicity for fabrication of diffraction holograms," Appl. Surf. Sci. **453**, 449–456 (2018).
23. N.L. Kazanskiy, V.A. Andreev, A.V. Bourdine, V.A. Burdin, O.G. Morozov, and A.H. Sultanov, "Modeling diffractive optics elements and devices," Proc. SPIE **10774** 107740O (2018).
24. J. E. Harvey and R. N. Pfisterer, "Understanding diffraction grating behavior: including conical diffraction and Rayleigh anomalies from transmission gratings," Opt. Eng. **58**(08), 1 (2019).
25. J. E. Harvey, C. L. Vernold, A. Krywonos, and P. L. Thompson, "Diffracted radiance: a fundamental quantity in nonparaxial scalar diffraction theory," Appl. Opt. **38**(31), 6469–6481 (1999).
26. V. E. Johansen, J. Andkjaer, and O. Sigmund, "Design of structurally colored surfaces based on scalar diffraction theory," J. Opt. Soc. Am. B **31**(2), 207–217 (2014).
27. CIE: International Commission on Illumination, http://www.cie.co.at/.
28. J. Wang, W. Liao, and P. Guo, "Modulated ultrasonic elliptical vibration cutting for ductile-regime texturing of brittle materials with 2-D combined resonant and non-resonant vibrations," International Journal of Mechanical Sciences **170**, 105347 (2020).